A Proposal to PAC34: G_{Ep}/G_{Mp} with an 11 GeV electron beam

E.J. Brash (co-spokesperson), D. Doughty, D. Heddle, Y. Prok
Christopher Newport University and Jefferson Lab

M.K. Jones (co-spokesperson), P. Bosted, S. Covrig, D. Gaskell, D. Higinbotham, T. Horn, W. Luo, D. Mack, G. Smith, W. Vulcan, B. Wojtsekhowski, and S. Wood
Jefferson Lab

V. Punjabi (co-spokesperson), W. Hinton, M. Khandaker
Norfolk State University

C.F. Perdrisat (co-spokesperson), M. Meziane, L.P. Pentchev
College of William and Mary

K. Aniol, D. Margaziotis
California State University, Los Angeles

E. Tomasi
IRFU, SPhN, CEA Saclay

W. Boeglin, S. Dhamija, P. Markowitz, J. Reinhold
Florida International University

J.R.M. Annand, D.J. Hamilton
University of Glasgow

M. Kohl, Y. Li
Hampton University

A.M. Davidenko, Yu.M. Goncharenko, V.P. Kubarovsky, Yu.M. Melnik, V.V. Mochalov, L.F. Soloviev, and A.N. Vasiliev
Institute for High Energy Physics, Protvino, Russia

N. Piskunov, D. Kirillov, I. Sitnik, J. Mushinsky, S. Basylev, V. Slepnev, I. Slepnev, G. Meshcheryakov, A. Nagaytsev, and I. Savin
Laboratory for High Energy, JINR, Dubna, Russia

Yu. Zanesvky, S. Chernenko, D. Fateev, and S. Razin
Detector Research Group
Laboratory for High Energy, JINR, Dubna, Russia

M. Mihovilovic, M. Potokar, S. Širca
Institute Jožef Stefan

W. Bertozzi, S. Gilad, A. Puckett
Massachussetts Institute of Technology

J. Calarco
University of New Hampshire

A. Ahmidouch, S. Danagoulian, A. Gasparian, P. Ambrozewicz
North Carolina A&T University

L. Gan
University of North Carolina at Wilmington

A. Daniel, P. King, J. Roche
Ohio University

C. Butuceanu, G.M. Huber. Z. Papandreou
University of Regina, Canada

R. Gilman, C. Glashausser, G. Kumbartzki, R. Ransome
Rutgers University

J. Lichtenstadt, E. Piasetzky, I. Pomerantz, G. Ron
Tel Aviv University

S. Strauch
University of South Carolina

H. Baghdasaryan, D. Day, M. Shabestari, R. Subedi, X. Zheng
University of Virginia

F.R. Wesselmann
Xavier University of Louisiana

S. Abrahamyan, A. Asaturyan, S. Mayilyan, A. Mrktchyan, H. Mkrtchyan, A. Shahinyan, V. Tadevosyan, and H. Voskanyan
Yerevan Physics Institute, Armenia

Abstract

We propose to measure the elastic form factor ratio of the proton, G_{Ep}/G_{Mp}, up to $Q^2 = 13\ GeV^2$ by polarization transfer. The proposed experiment uses exclusively instrumentation which will exist shortly after the 11 GeV beam becomes available in Hall C, namely the SHMS, and BigCal. The SHMS will be equiped with the existing Focal Plane Polarimeter (FPP), recently used in the Gep-III experiment. BigCal was also used in the Gep-III experiment, and both instruments performed very well during the six month duration of that experiment.

The physics interest in continuing these measurements of the form factor ratio to the largest possible Q^2 is manyfold. The data we propose to obtain will serve as direct challenges of all models of the nucleon, from phenomenological, QCD-inspired models, such as Vector Meson Dominance and Relativistic Constituent Quark Models, to more fundamental QCD lattice calculations or solutions of the Dyson-Schwinger field equations. The data will also test the limits of the Chiral Quark Soliton Model and contribute to the determination of one of the Generalized Parton Distributions.

This proposal is based on a Letter of Intent, LOI12-06-103 "GEp/GMp" with an 11 GeV beam", which was favorably received by PAC30.

1 Introduction

In many senses, the internal structure of the nucleon is the defining problem of QCD, the fundamental theory of the strong interaction. The internal structure of the nucleon defines its mass, spin, and its interactions. The nucleon is the fundamental building block of the nucleus, and indeed it is the residual nucleon-nucleon interaction that governs all nuclear structure, in much the same way that residual interactions between atoms governs molecular structure. As such, a full and detailed quantitative understanding of the internal structure of the nucleon is a necessary precursor to extending our understanding of nuclear physics.

Based on more than a half-century of experimental and theoretical effort, we have made significant progress in our understanding of nucleon structure. At short distances, the quarks inside the nucleon are nearly unbound; this is the region of asymptotic freedom, where the quark-quark interaction is feeble. As a result, the interaction may be treated perturbatively, and the theory known as pQCD (perturbative QCD) describes a wealth of experimental data extremely well. However, at larger distances, quarks are strongly bound; this is the region of quark confinement, where QCD becomes complex, and exact quantitative calculations are exceedingly difficult.

A fundamental test of the QCD in the confinement region is the electromagnetic structure of the nucleon. In particular, measurements of the elastic electric and magnetic form factors of the proton, G_{Ep} and G_{Mp}, respectively, at large momentum transfer, Q^2, shed new light on its internal nonperturbative structure. To this point, we have relied primarily on models to attempt to describe the data. In recent years, lattice QCD has emerged as a theory which holds great promise. We note, for example, recent calculations [1, 2] of the nucleon electromagnetic form factors on the lattice; while this represents a significant step forward, much work still remains to be done before meaningful quantitative comparisons between the data and unquenched lattice QCD calculations can be made.

2 Current Status of the Experimental Data

The ratio, $R_p = \mu_p G_{Ep}/G_{Mp}$, where μ_p is the proton magnetic moment, has been measured extensively over the last several decades using two experimental techniques. In the Rosenbluth separation method, one measures the angular dependence of the $e-p$ scattering cross section at a fixed value of Q^2. The results are consistent with $R_p \approx 1$ for $Q^2 < 6$ GeV^2 [3, 4, 5, 6]. In dramatic contrast, a series of experiments at Jefferson Lab in 1998-2000 [7, 8, 9, 10], using the polarization transfer method, where one measures R_p directly by measuring the ratio of transverse to longitudinal polarizations of the recoiling proton, have revealed that the ratio decreases approximately linearly with increasing Q^2 over the same momentum range. The polarization transfer results are of unprecedented high precision and accuracy, due in large part to the small systematic uncertainties associated with the experimental technique, and cannot currently be reconciled with the Rosenbluth separation results. These 1998-2000 results were unexpected, and have stimulated an onslaught of theoretical papers on the subject; they are among the most often quoted results form Jefferson Lab.

One possible reason for the observed discrepancy lies in the radiative corrections which are very important for Rosenbluth cross sections, but much less so for the polarization results. The LT separation technique extracts the ratio, R_p, from the ϵ dependence of the cross

section at fixed Q^2. With increasing Q^2, the cross section is increasingly dominated by G_{Mp}, and the relative contribution of G_{Ep} decreases. Hence, the ϵ dependence of the radiative correction becomes increasingly important to the process of extracting the form factors correctly at high Q^2. In contrast, what is measured in polarization transfer experiments is a ratio of cross sections, corresponding to longitudinal and transverse polarization, and both are affected similarly by radiative effects; it is this subtle cancellation effect that results in only an extremely weak dependence on radiative corrections. Although the G_{Ep} "crisis" has not been entirely resolved at this time, it appears likely that a combination of more careful calculations of the standard contributions to radiative corrections, and inclusion of the previously ignored two-hard-photon contribution, might fully explain it (See, for example, Refs. [11, 12, 13, 14]).

A third G_{Ep}/G_{Mp} experiment, Gep-III (E-04-108) was completed in June of 2008 in Hall C [15]. It extends the Q^2-range from 5.6 to 8.54 GeV^2. Fig. 1 shows the preliminary data at 4 values of Q^2: 2.5 GeV^2, where we studied the ϵ-dependence of G_{Ep}/G_{Mp}, 5.2 GeV^2 which was a test point and used to check the spin transport procedure, and two new values, 6.8 and 8.54 GeV^2. Although preliminary, these results confirm the Hall A results once more, and give a strong hint that the ratio keeps decreasing with Q^2, at approximately the same rate, or faster. G_{Ep}/G_{Mp} appears to be crossing zero between 7 and 8 GeV^2. These preliminary results, together with the earlier ones, indicate clearly that we are not close to the pQCD regime, but rather in a regime dominated by soft physics (see, for example, the discussion in subsequent sections on the scaling behavior of F_2/F_1).

Also shown in Fig. 2 are the preliminary results of E-04-019 [16], which measured the ratio G_{Ep}/G_{Mp} by recoil polarization at fixed Q^2 (2.5 GeV^2), for 3 values of ϵ, to check the validity of the Born approximation (or to detect the contribution of the two hard photon process). The ratio should be ϵ-independent- and appears to be so at the level of the current error bars.

There has been a new experiment in Hall C to detect non-linearity in the Rosenbluth plot with unprecedented small error bars [17]; the results are not available at this time. This is another attempt to directly detect a predicted contribution of the two hard photon process.

3 Summary of Theoretical Progress

To date, all theoretical models of the nucleon form factors are based on effective theories; they all rely on a comparison with existing data and their parameters are adjusted to fit the data. The much improved quality of the polarization data from JLab, compared to the Rosenbluth data has made a significant impact on theoretical models. Still, as we will see, the comparatively limited range of dynamic coverage of the form factor data results in large model uncertainties in many cases.

In the following sections, we discuss a number of distinct theoretical approaches; the list is not all inclusive; for a more complete review, see Ref. [18]. In some cases, these calculations could be considered to be "first principle" calculations of the form factors. In others, a more phenomenological approach is taken, in the hopes of gaining a more intuitive understanding of nucleon structure.

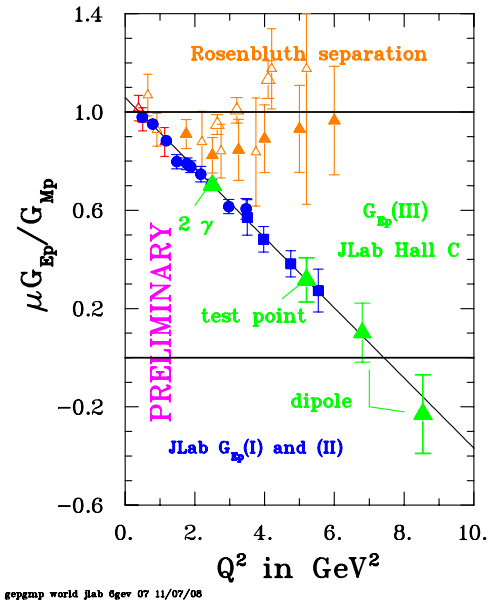

Figure 1: *The preliminary results from Gep-III. These results have been extracted from the data using a spin transport matrix for the HMS which assumes that the HMS is simply a dipole magnet. Also shown are the Hall A, 1998-2000 polarization results (blue circles and squares) [7, 8, 10], all Rosenbluth cross section separation results (orange symbols),and the preliminary results of the recently completed Gep-III experiment in Hall C (green triangles)[15].*

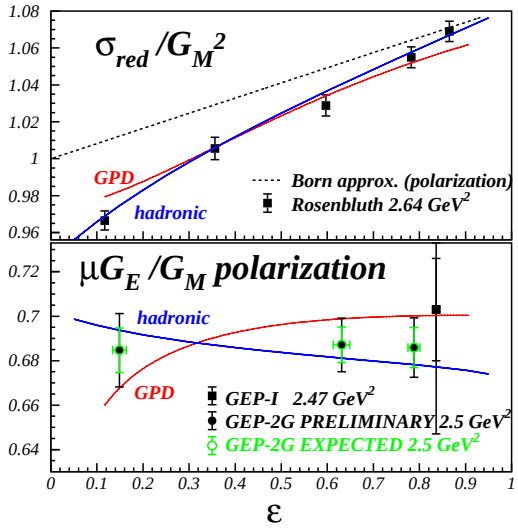

Figure 2: *The preliminary results from the two gamma experiment. In the top panel the reduced cross section prediction from [11] and [12]. Bottom panel $\mu_p G_{Ep}/G_{Mp}$ from the recent two gamma recoil polarization experiment in Hall C. Black error bars are preliminary, green error bars are predicted final. The same theoretical predictions are shown as in the top panel.*

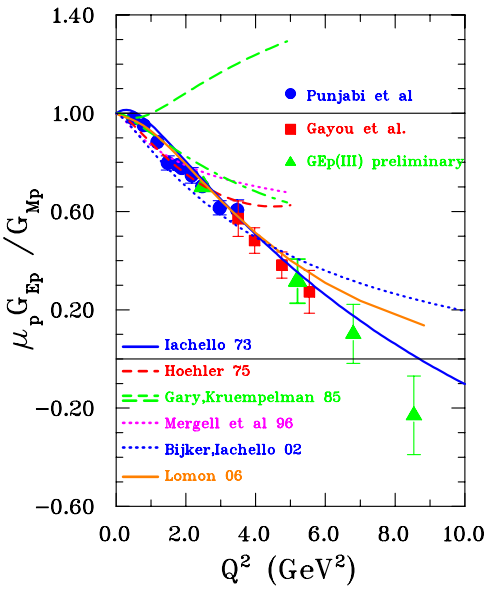

Figure 3: *Comparison of Vector Dominance Model (VMD) fits with the same data of Ref. [7, 10] and Ref. [8]; preliminary results of Gep-III included.*

3.1 Vector Meson Dominance

The earliest models to explain the global features of the nucleon form factors, were vector meson dominance (VMD) models. In this picture the photon couples to the nucleon through the exchange of vector mesons. Such VMD models are a special case of more general dispersion relation fits, which allow to relate time-like and space-like for factors.

The lowest lying hadrons with vector quantum numbers are the vector mesons $\rho(770)$, $\omega(782)$ and $\phi(1020)$. These vector mesons are seen as prominent resonances at the corresponding values of the e^+e^- squared CM energy and $Q^2 < 0$. It follows that these low lying resonances in the time-like region dominate electron scattering in the space-like domain for $Q^2 > 0$. A large class of models for F_1 and F_2 are based on this vector meson dominance (VMD) hypothesis.

An early VMD fit by Iachello *et al.* [19] predicted a linear decrease of the proton G_{Ep}/G_{Mp} ratio, in basic agreement with the result from the polarization transfer experiments. Such VMD models have been extended by Gari and Krümpelmann [20] to include the perturbative QCD (pQCD) scaling relations of Brodsky and Farrar [21] for the nucleon electromagnetic form factor.

In more recent years, extended VMD fits which provide parametrization of all nucleon e.m. form factors have been obtained. An example is Lomon's fit [22], which uses $\rho(770)$, $\omega(782)$, $\phi(1020)$, and $\rho'(1450)$ mesons and contains 11 parameters. Another such recent parametrization by Bijker and Iachello [23] including $\rho(770)$, $\omega(782)$, and $\phi(1020)$ mesons only achieves a good fit by adding a phenomenological contribution attributed to a quark like intrinsic qqq structure (of rms radius ~ 0.34 fm) besides the vector-meson exchange terms. The pQCD scaling relations are built into this fit which has 6 free parameters which are fit to the data. Unlike the early fit of Ref. [19], the new fit of Ref. [23] gives a very good

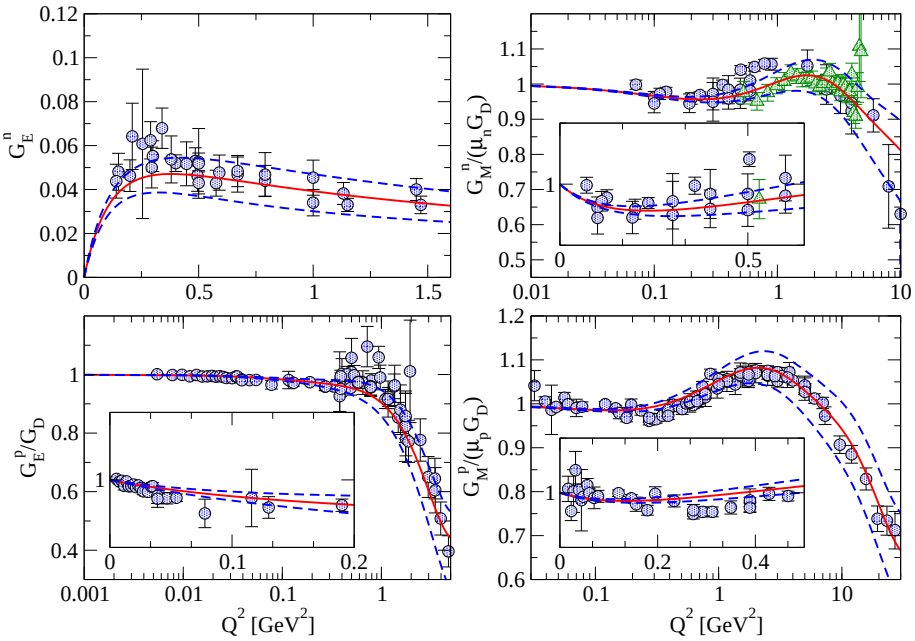

Figure 4: *Dispersion relation (15 parameter) fit for the four nucleon (space-like) e.m. FFs compared with the world data (circles) including the JLab/CLAS data for G_{Mn} (triangles) [29]. The dashed curves indicate the 1σ deviation from the fit, given by the solid curves. Figure from Ref. [28].*

description of the neutron data at the expense of a somewhat worse fit for the proton data.

Despite the relatively good fits obtained by the VMD models, such an approach is at odds with general constraints from unitarity. This problem can be repaired with the use of dispersion relations. Assuming an unsubtracted dispersion relation, the nucleon e.m. form factors $F(q^2)$, can be obtained as :

$$F(q^2) = \frac{1}{\pi} \int_{t_0}^{\infty} dq'^2 \, \frac{\mathrm{Im}F(q'^2)}{q'^2 - q^2}. \tag{1}$$

Dispersion analyzes are performed separately for nucleon isoscalar and isovector form factors. In the vector-isovector spectral function one notices a large non-resonant contribution starting from $t_0 = 4m_\pi^2$ and extending under the ρ-peak; it is due to the two-pion continuum. For the isoscalar spectral function, the integral starts at $t_0 = 9m_\pi^2$, corresponding with 3π intermediate states. The two-pion continuum contribution was estimated by Höhler and collaborators [24] by using pion time-like FF data and $\pi\pi \to N\bar{N}$ amplitudes.

Höhler's analysis has been updated by Mergell, Meissner, and Drechsel [25] in the mid-nineties and extended to include the nucleon time-like FF data [26]. The inclusion of recent neutron FF data in such dispersion relation analysis has been performed in Ref. [27]. The resulting analysis describes the nucleon isovector form factors through the 2π continuum (including the $\rho(770)$), and three additional vector isovector meson poles : $\rho'(1050)$, $\rho''(1465)$, $\rho'''(1700)$. The isoscalar FFs are described by four vector isoscalar meson poles : $\omega(770)$, $\phi(1020)$, $S'(1650)$ and $S''(1680)$.

The dispersion relation analysis has been further improved by Belushkin *et al.* [28]. In addition to the 2π continuum present in the isovector spectral functions, also the $\rho\pi$ and $K\bar{K}$ continua were included as independent input in the isoscalar spectral functions. In Ref. [28], the 2π continuum was reevaluated using the latest experimental data for the pion form factors in the time-like region. A simultaneous fit to the world data for all four form factors in both the space-like and time-like regions was performed. For G_{Ep}/G_{Mp} at larger Q^2 the JLab/Hall A polarization data have been used, and for G_{Mn} the preliminary JLab/CLAS data [29] have been included. The resulting 15 parameter fits are seen in Fig. 4.

3.2 Relativistic Constituent Quark Models

In the constituent quark model, the nucleon consists of three constituent quarks, which are thought to be valence quarks dressed with gluons and quark-antiquark pairs that are much heavier than the QCD Lagrangian quarks. All other degrees of freedom are absorbed into the masses of these quarks. The early success of the non-relativistic constituent quark model was in describing the spectrum of baryons and mesons with correct masses [30]. However, to describe the elastic form factor data in terms of constituent quarks, it is necessary to include relativistic effects because the momentum transfers involved are up to ten times larger than the constituent quark mass.

In the earliest study of the relativistic constituent quark models (rCQM), Chung and Coester [31] calculated electromagnetic nucleon form factors with Poincaré-covariant constituent-quark models and investigated the effect of the constituent quark masses, the anomalous magnetic moment of the quarks, and the confinement scale parameter; the prediction is shown as a red dotted curve in Fig. 5. Although somewhat difficult to see in Fig. 5, the agreement with the data over the range of Q^2 of the calculation is remarkable; in particular we note that the general trend of decreasing form factor ratio with increasing Q^2 is closely connected with the inclusion of relativistic effects.

Subsequently, Frank $et\ al.$ [32] had calculated G_{Ep} and G_{Mp} in the light-front constituent quark model and predicted that G_{Ep} might change sign near 5.6 GeV^2; this predicted value is inconsistent with the current data. The calculation used the light-front nucleonic wave function of Schlumpf [33]. The light-front dynamics can be seen as a Lorentz transformation to a frame boosted to the speed of light. Under such a transformation, the spins of the constituent quarks undergo Melosh rotations. These rotations, by mixing spin states, play an important role in the calculation of the form factors. The results of their calculation are shown as the thick black solid curve in Fig. 5. The importance of this calculation lies primarily in the notion that intrinsic spin is itself a relativistic effect, and thus a comparison of the data to such calculations help us to disentangle for example the relativistic dynamics from other intrinsic nucleon structure effects.

Several calculations with the rCQM have been motivated specifically by the data from the JLab experiments [34, 35, 36, 37]. Cardarelli *et al.* [34] calculated the ratio with light-front dynamics and investigated the effects of SU(6) symmetry breaking. They showed that the decrease in the ratio with increasing Q^2 is due to the relativistic effects generated by Melosh rotations of the constituent quark's spin (short dot-dashed cyan curve in Fig. 5). In Ref. [35], they pointed out that within the framework of the rCQM with the light-front formalism, an effective one-body electromagnetic current, with a proper choice of constituent quark form

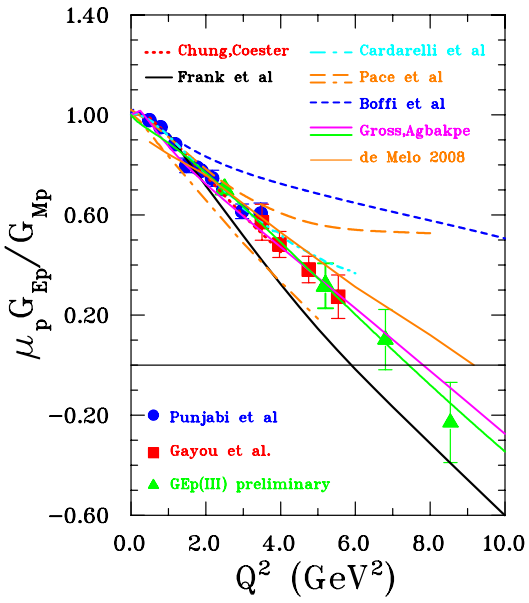

Figure 5: *Comparison of constituent quark model (CQM)calculations with the data of Ref. [7, 10] and Ref. [8]; preliminary data from Gep-III included.*

factors, can give a reasonable description of pion and nucleon form factors. The results of their calculation with two different quark form factors are shown as the orange dot-dashed and dashed curves in Fig. 5. It is interesting to note that the two calculations begin to diverge significantly from one another, and from the data, with increasing Q^2. This highlights how accurate and precise data at large Q^2 can serve to further constrain such models, and thus provide a deeper understanding of the underlying structure.

De Sanctis *et al.* [36] have calculated the ratio G_{Ep}/G_{Mp} within the hypercentral constituent quark model including relativistic corrections: however, the slope of their G_{Ep}/G_{Mp} ratio is too small by a factor of $\sim$2. The chiral constituent quark model based on Goldstone-boson-exchange dynamics was used by Boffi *et al.* [37] to describe the elastic electromagnetic and weak form factors. They compute these form factors in a covariant framework using the point-form approach to relativistic quantum mechanics. The results of these calculations are shown as the blue short dashed curve in Fig. 5.

Miller [38] has used a model proton wave function, constructed using Poincaré invariance and constrained by the JLab data, to study the shape of the proton. Interestingly, Miller puts forward the idea that a non vanishing sum of the orbital angular momentum of the quarks of the proton is indicated by non-spherical shapes. By evaluating the rest frame ground state matrix elements of spin-dependent charge density operators, he concludes that for high momentum quarks with spins aligned either parallel or anti-parallel to the proton spin, a non-spherical shape results.

Subsequently, Gross and Agbakpe [39] revisited the rCQM imposing the condition that the constituent quarks become point particles as $Q^2 \rightarrow \infty$ as required by pQCD. Using a covariant spectator model which allows exact handling of all Poincaré transformations, and monopole form factors for the constituent quarks, they obtain excellent ten parameter fits to all four nucleon form factors (shown as magenta and green solid curves in Fig. 5). They

conclude that the recoil polarization data can be fitted with a spherically symmetric state of three constituent quarks.

Most recently, Kvinikhidze and Miller [40] have shown that the Gross and Agbakpe model of the nucleon contains non-spherical shapes; they conclude that it is the use of the $spin-dependent$ density operator which is key to revealing these features. Finally, they point out that deviations from a spherical shape are associated physically with the motion of the spin-$\frac{1}{2}$ quarks moving relativistically within the proton. This conclusion has been contested by Gross, Ramalho and Pe$\check{n}$a [41].

A recent result obtained by de Melo *et al* [42] takes into account effects of non-valence quarks, in a light-front context. They show that the contribution of $q\overline{q}$ pairs, resulting from the Z-diagram, when added to the valence quark contribution, generates a zero crossing of the G_{Ep}/G_{Mp} ratio near 8 GeV^2 (see orange solid line in Fig. 5).

The main conclusions that we draw from the comparison of the various models to the data in Fig.5 are:

- The models are certainly beginning to diverge from one another as Q^2 increases. Thus, new accurate and precise data at large values of Q^2 will serve to severely constrain these models.

- We have seen that through a comparison of the data to the various models, and through the procedure of tuning these models to the data, we are able to gain new and important information regarding dynamical effects, as well as the underlying nucleon structure. Moreover, the availability of accurate and precise data to as large a value of Q^2 as possible helps us to disentangle these effects from one another.

3.3 Asymptotic Behavior

The fundamental ratio of Pauli to Dirac form factors, F_{2p}/F_{1p}, can be directly obtained from the measured ratio G_{Ep}/G_{Mp}. At very large momentum transfers, in the perturbative QCD domain, one expect the long standing prediction of Brodsky and Farrar [21], $Q^2F_{2p}/F_{1p} \approx \ constant$ to be valid; a direct consequence of the fact that hard scattering processes dominates. The experimental results, which are shown in Fig. 6 clearly show that we have not reached the pQCD region, as scaling has not been observed.

Recently there have been two revisions of the pQCD prediction for the large Q^2 behavior of F_2. In the first, Brodsky [43] argues that the pQCD motivated behavior of F_2 must contain an extra logarithmic term from higher twist contributions; the 3 free parameters a, b and c of the expression

$$\frac{F_{2p}}{F_{1p}} = \frac{1}{1 + (Q^2/c)\ln^b(1 + Q^2/a)} \tag{2}$$

were fitted in Ref. [43] to the data presented here augmented from the data of Ref. [8]. In the second, Belitsky $et\ al.$ [44] reiterate the fact that the spin of a mass-less (or very light) quark cannot be flipped by the virtual photon of the ep reaction. For a quark to undergo spin-flip, it must be in a state of non-zero angular momentum with projection $\mid L_z \mid$=1. As a result, the standard pQCD prediction for F_{2p} (namely $\propto Q^{-6}$) becomes modified by a logarithmic

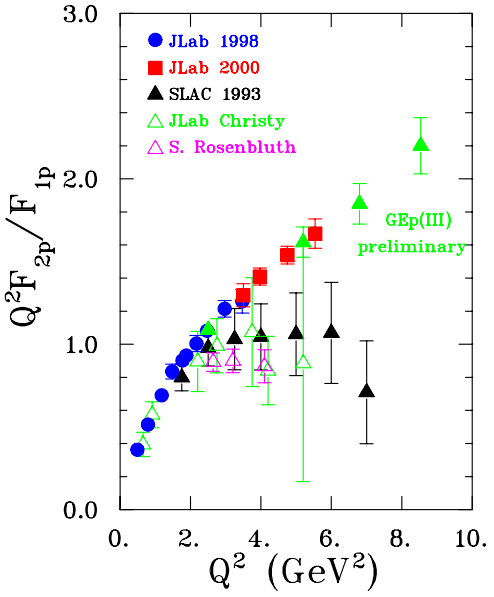

Figure 6: *The ratio Q^2F_2/F_1 from various data sets.*

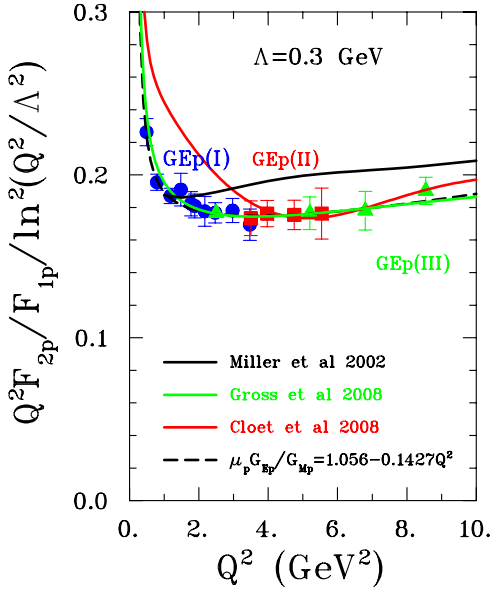

Figure 7: *The ratio Q^2F_2/F_1 over $ln^2\frac{Q^2}{\Lambda^2}$, compared to calculations from [32, 41, 61]*

.

term such that:

$$\frac{F_{2p}}{F_{1p}} = \frac{A}{\kappa_p Q^2}\ln^2(\frac{Q^2}{\Lambda^2}), \tag{3}$$

where A is a normalization constant; Λ is a cutoff constant required to suppress the infrared singularity generated by the very soft part of the quark wave function. Although the constant A in the expression above is not determined, a fit to the data of this paper augmented by the data of [8] gives $\Lambda = 300$ MeV, and A =0.175. The soft physics scale of the nucleon is determined by Λ; its size is of order of the transverse quark momentum in the nucleon. In Fig. 7 $\frac{Q^2F_{2p}/F_{1p}}{\ln^2(Q^2/\Lambda^2)}$ is shown, indicating approximate scaling above 2 GeV^2. The three theoretical curves shown in this figure are explained elsewhere in this document.

Inspired by the results of JLab polarization experiments, Ralston and Jain [45], revisited the calculation of the single-quark spin-flip amplitude responsible for the Pauli form factor in the framework of QCD and concluded that if quarks in the proton carry orbital angular momentum, then F_{2p}/F_{1p} should behave like $\frac{1}{\sqrt{(Q^2)}}$, rather than the well known pQCD prediction of $\frac{1}{Q^2}$ (Ref. [21]). In a different approach, Miller and Frank [46] have shown that imposing Poincaré invariance leads to violation of the helicity conservation rule, which results in the behavior of F_{2p}/F_{1p} observed in the JLab data.

3.4 Generalized Parton Distributions

The Generalized Parton Distributions (GPDs), introduced nearly a decade ago, represent a framework within which hadrons are described in terms of quark and gluonic degrees of

freedom (See, for example, Refs. [47, 48, 49, 50]) . They combine together the concepts of form factors, parton densities, and distribution amplitudes, and as such serve as an extremely useful tool in studies of hadronic structure.

It turns out that the elastic electromagnetic form factors of nucleons are related to moments of the GPDs and therefore offer important constraints on the GPDs themselves, and thus in turn constrain our description of the nucleon's structure. The nucleon Dirac, F_1, and Pauli, F_2 form factors are the zeroth moments of the $H(x,t)$ and $E(x,t)$ GPDs :

$$F_1(t) = \sum_q e_q F_1^q(t) \qquad F_2(t) = \sum_q e_q F_2^q(t) \tag{4}$$

$$F_1^q(t) = \int_{-1}^{+1} dx H^q(x,\xi,t) \qquad F_2^q(t) = \int_{-1}^{+1} dx E^q(x,\xi,t) \tag{5}$$

in which q are the quark flavors, ξ is the skewness, and t is the momentum transfer. In an early use of GPDs to describe the nucleon form factor, F_1, Radyushkin [47] parametrized the H GPD with a Gaussian form and was able to fit the existing data with only a single parameter. When precision data from the JLab experiments for F_2/F_1 up to Q^2=3.5 GeV^2 became available, Afanasev [48] extended the approach of Radyushkin and included a determination of the E GPD. This was the first attempt to extract information on the angular momentum of the valence quarks and indicated a need to measure F_2/F_1 to large Q^2 in order to determine the x dependence of the E GPD. Using the most recent JLab data for F_2/F_1 for the proton up to Q^2=5.6 GeV^2 and for the neutron F_2/F_1 up to Q^2=1.5 GeV^2, two theoretical groups [49, 50] have fitted H and E GPDs to the existing nucleon form factor data.

The form factors are independent of the skewness, ξ, which simplifies the GPD integrals, in contrast to deeply virtual exclusive (DVE) reactions. While GPD formalism for DVE reactions is limited to low t, the GPD formalism for the form factors is applicable to high t, and thus form factor measurements at high t (large Q^2) are ideally complementary to the DVE experiments. The invariant t depends on both the longitudinal and transverse components of the momentum transferred to the nucleon. Therefore, form factor measurements at high t allow unique access to the small transverse momentum structure of the nucleon.

By introducing non-forward parton densities :

$$\mathcal{H}^q(x,t) = H^q(x,0,t) + H^q(-x,0,t) \tag{6}$$

$$\mathcal{E}^q(x,t) = E^q(x,0,t) + E^q(-x,0,t) \tag{7}$$

the integrals in Eqns. 4 and 5 can be reduced to integrals over $0 < x < 1$. The $\mathcal{H}^q(x,t)$ are equal to the valence quark densities, $u_v(x)$ and $d_v(x)$, in the limit of $t \to 0$. But the $\mathcal{E}^q(x, t = 0)$ cannot be directly expressed in terms of any known parton distribution. New information about the transverse momentum distribution of the quarks in the nucleon is contained in $\mathcal{E}^q(x, t = 0)$. Just as the normalization integrals for the $\mathcal{H}^q(x,t)$ are related to the charge of the quarks, the normalization integrals for $\mathcal{E}^q(x, t = 0)$ must equal their anomalous magnetic moment.

Burkhardt [51] introduced the concept that Fourier transforms of the GPDs at $\xi = 0$ describe the distribution of partons in the transverse plane. The form factors are non-forward matrix elements of the current operator, and describe how the charge (i.e. the forward matrix element of the same operator) is distributed in position space. By analogy, as off-forward

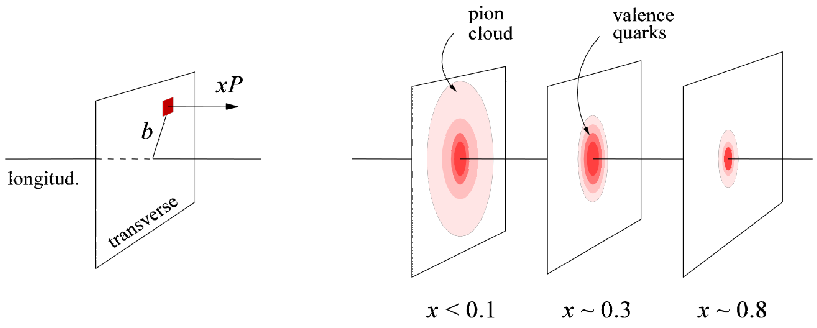

Figure 8: *Schematic representation of the transverse position of partons in the target nucleon, for various values of x. (prepared by C. Weiss, for the JLab 12GeV CDR)*

matrix elements, the GPDs contain information about how the parton distribution functions (PDFs) are distributed in position space. While conventional PDFs contain no information about the spatial distribution of partons, if one knows the GPDs for $\xi = 0$, one can simultaneously determine the longitudinal momentum and transverse position of partons in the target nucleon, as depicted in Fig. 8, as functions of transverse position, for various values of x.

One of the most interesting constraints that nucleon elastic form factor data at large Q^2 can provide relates to the issue of the various contributions from quarks, gluons, and orbital angular momentum to the total angular momentum of the nucleon. A quark of flavor q in the nucleon has a total angular momentum, J^q, which is related to the GPD's H^q and E^q by the sum rule [52] :

$$2J^q = \int_{-1}^{1} x\{H^q(x,0,0) + E^q(x,0,0)\}dx \tag{8}$$

In Ref. [49], $\mathcal{H}^q(x,t)$ is parametrized in modified Regge form as

$$\mathcal{H}^q(x,t) = q_v(x)x^{-\alpha_1(1-x)t} \tag{9}$$

The $q_v(x)$ are the known parton distributions, so $\mathcal{H}^q(x,0,0)$ is simply given by $q_v(x)$. $\mathcal{E}^q(x,0,0)$ is unknown and, in Ref. [49], $\mathcal{E}^q(x,t)$ is parametrized as:

$$\mathcal{E}^q(x,t) = \frac{\kappa_q}{N_q}(1-x)^{\eta_q} q_v(x) x^{-\alpha_2(1-x)t} \tag{10}$$

in which N_q is a normalization fixed by $\kappa_q = \int_0^1 \mathcal{E}^q(x,0)dx$. Fitting the nucleon form factor data determines the coefficient α_1 of $\mathcal{H}^q(x,t)$ and the coefficients, α_2, η_u and η_d in $\mathcal{E}^q(x,t)$. A good fit is obtained to the nucleon magnetic form factors and the ratio of the nucleon G_E/G_M has a better fit with the extra η_u and η_d parameters. The η_u and η_d parameters define the large x behavior of $\mathcal{E}^q(x,t)$ which is determined from the large t dependence of F_2^p/F_1^p.

Neglecting the sea quark contribution, the contribution of the u and d valence quarks to the total angular momentum can be calculated. Ref. [49] obtains $2J^u = 0.63$ and $2J^d =$

-0.06 which agrees with quenched lattice QCD calculations. The intrinsic spin contribution of the valence quark, Δq_v, is known from the PDFs, so the orbital angular momentum of the quark can be calculated according to $2L^q = 2J^q - \Delta q_v$. Over the coming years, with the projected availability of reliable un-quenched lattice QCD calculations, it will be desirable to have elastic form factor data at the highest Q^2 possible so that meaningful comparisons can be made between lattice QCD and GPD-based calculations.

3.5 Charge and Magnetization Densities

Considerable progress has been made in the last few years, in understanding the relationship between momentum space form factors, and position space charge and magnetization densities in the plane transverse to the momentum transfer. In particular Miller [54] has exploited the advances in the understanding and characterization of the GPDs, to derive a model independent, transverse density defined in the infinite momentum frame, from the form factors F_1.

Starting from the relation between the form factor $F_1(t)$ and the GPD $H_q(x,t)$,

$$F_1(t) = \sum_q e_q \int dx H_q(x,t) \tag{11}$$

and the relation between the parton distribution $q(x,\vec{b})$ and the GPD $H_q(x,t)$:

$$q(x,\vec{b}) = \int \frac{d^2q}{(2\pi)^2} e^{i\vec{q}.\vec{b}} H_q(x, t=-q^2). \tag{12}$$

and after a few (non-trivial) steps the transverse density ρ_{perp} can be written in terms of the form factor F_1 and impact parameter $\vec{b}$ as follows:

$$\rho_{perp}(b) = \sum_q \int dx q(x,\vec{b}) = \int \frac{d^2q}{(2\pi)^2} F_1(Q^2=q^2) e^{i\vec{q}.\vec{b}} \tag{13}$$

$$\text{which is rewritten as } \rho_{perp}(b) = \int \frac{QdQ}{(2\pi)} J_0(Qb) \frac{G_E(Q^2) + \tau G_M(Q^2)}{1+\tau}, \tag{14}$$

where J_0 is a spherical- Bessel function.

Using two of the available data parametrizations for G_E and G_M the authors then obtain, in the infinite momentum frame, the perpendicular (to the momentum transfer) charge distribution for the proton and neutron shown in the upper two panels of Fig. 9. The unexpected feature is the negative value of ρ_{perp} at small distances ($< 0.4fm$) for the two dimensional charge distribution of the neutron. In a detailed discussion (which assumes isospin symmetry) the authors then proceed to relate this behavior to the different distributions for the two light quark flavors, u and d, shown in the lower panel of Fig. 9.

3.6 QCD Solutions

Lattice QCD calculations of nucleon structure quantities provide *ab initio* evaluations of quantities such as the nucleon electromagnetic form factors from the underlying theory of QCD.

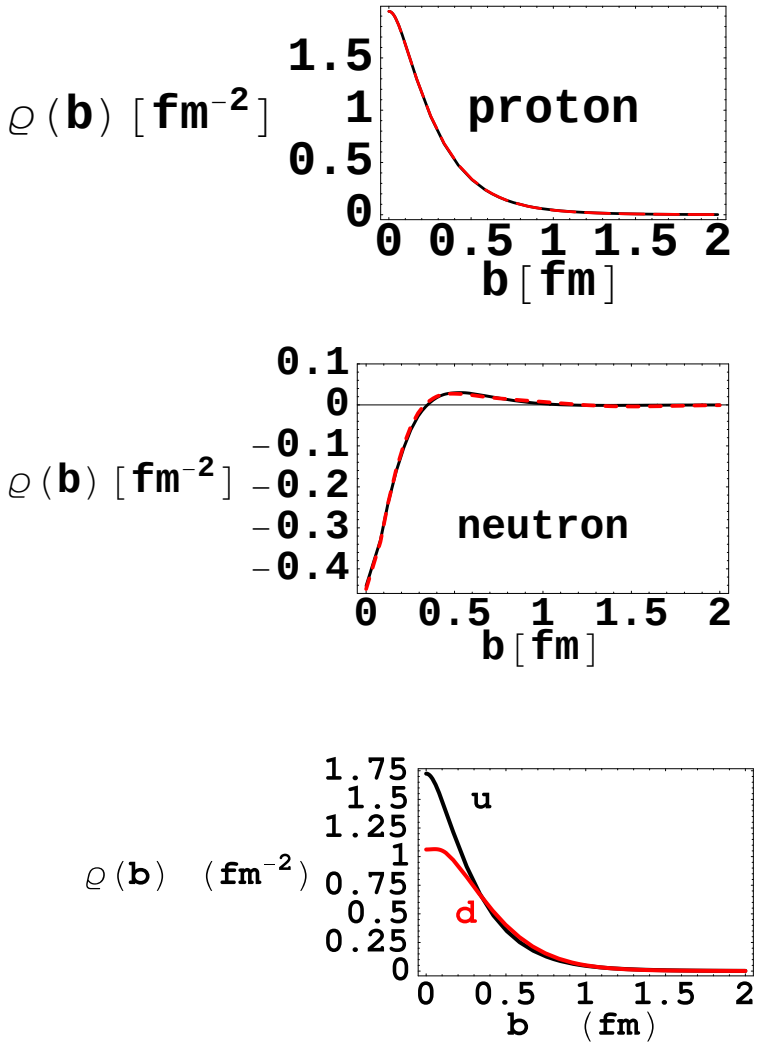

Figure 9: *Upper Two Panels: The transverse charge densities of the proton and neutron, $\rho_{perp}(b)$, according to Ref. [54]. The two different curves correspond to two different parametrizations of the form factors. Lower Panel: The transverse charge densities for u and d quarks, according to Ref. [54]. Both curves are normalized to unity.*

Lattice QCD is a discretized version of QCD formulated in terms of path integrals on a space-time lattice [55] with the only parameters, in principle, being the bare quark masses and the coupling constant. The continuum theory is obtained by extrapolating results obtained at some finite lattice spacing, a, down to $a = 0$, requiring separate calculations at several values of a.

Typically, the u and d quark masses used are larger than in the real world. This enables the inversion of the fermionic matrix, which is needed for the calculation of hadronic matrix elements, with currently available computing resources. To connect those results with reality requires extrapolation down to physical quark masses (in fact,m_q is proportional to m_π^2, and so typically calculations are evaluated as a function of m_π^2). This chiral extrapolation has only recently come down to pion mass values below 350 MeV [56, 57].

Lattice calculations for the (space-like) nucleon electromagnetic form factors require the evaluation of three-point functions, which involve two topologically different contributions: the connected and disconnected diagrams. Only the connected diagram contributes to the isovector combination of form factors $F^v = F^p - F^n$. Full QCD (un-quenched) results include both. The disconnected diagram requires a numerically more intensive calculation, and is at present neglected in most lattice studies. When taking the difference between proton and neutron electromagnetic form factors, i.e. for the isovector combination of nucleon electromagnetic form factors, the disconnected contribution drops out. Fig. 10 shows the m_π-mass dependence of the isovector form factor F_1^{u-d} obtained by the LHPC collaboration [58]; the solid line represents the data; the calculation is limited to small Q^2 values.

An encouraging effort to extrapolate lattice calculation results for G_{Ep}/G_{Mp} to the physical pion mass is due to Matevosyan *et al* [59]; they use the parameters of the light front cloudy bag model (LFCBM) of Miller [60] to extrapolate the lattice results of the QCDSF collaboration; the results are shown in Fig. 12.

A different approach is illustrated by deriving solutions to the Dyson-Schwinger equations to calculate form factors, a quantum field theoretical approach to hadron structure [61]. The mechanism for mass acquisition of the QCD quark to the dressed quark mass is related to the dynamical chiral symmetry breaking; it explains the mass growth with momentum as accretion of a gluon cloud. In Ref. [61] a parameter-free Faddeev equation for the nucleon is constructed, which describes the core of dressed quarks in the nucleon. A recent result for $\mu_p G_{Ep}/G_{Mp}$ is shown in Fig. 11. The fact that the calculation begins to agree with the data starting around 4 GeV^2 is related to the fact that the calculation omits the pseudo-scalar meson cloud contribution.

4 The Recoil Polarization Method

The relationship between the Sachs electromagnetic form factors and the degree of polarization transfer in ${}^1H(\vec{e}, e'\vec{p})$ scattering was first developed by Akhiezer and Rekalo [62], and later discussed in more detail by Arnold, Carlson, and Gross [41].

For single photon exchange, the transferred polarization can be written in terms of the Sachs form factors:

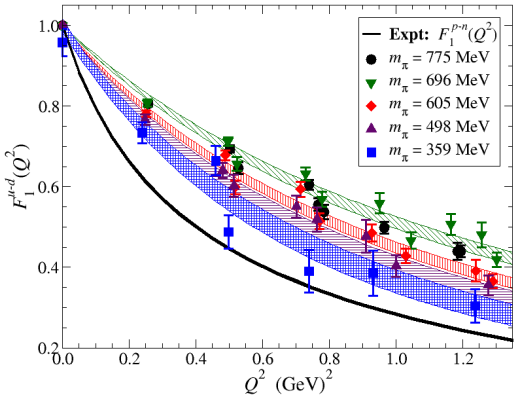

Figure 10: *Isovector form factor* $F_1^V = F_1^p - F_1^n$ *in lattice QCD[58]*

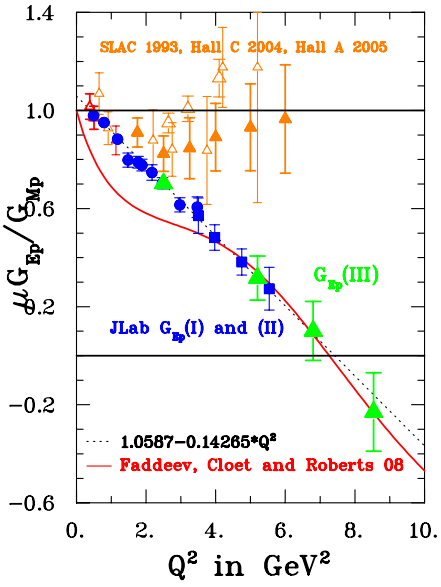

Figure 11: *Nucleon form factor as solution of parameter-free Poincare covariant Faddeev equ. [61]. Preliminary results from Gep-III included.*

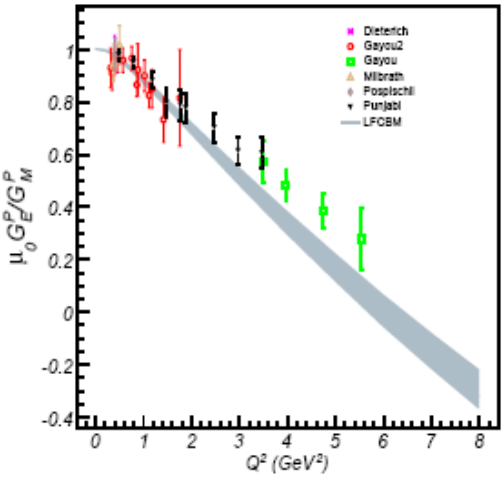

Figure 12: *The physical form factor ratio obtained by extrapolating to the physical pion mass, the lattice results of the QCDSF collaboration [59, 1].*

$$P_n = 0 \tag{15}$$

$$\pm h P_l = \pm h \left(\frac{E_e + E'_e}{M} \right) \frac{\sqrt{\tau(1+\tau)}\, G_{Mp}^2(Q^2)\, \tan^2 \frac{\theta_e}{2}}{G_{Ep}^2(Q^2) + \frac{\tau}{\epsilon_\gamma} G_{Mp}^2(Q^2)} \tag{16}$$

$$\pm h P_t = \mp h \frac{2\sqrt{\tau(1+\tau)}\, G_{Ep}\, G_{Mp}\, \tan \frac{\theta_e}{2}}{G_{Ep}^2(Q^2) + \frac{\tau}{\epsilon_\gamma} G_{Mp}^2(Q^2)} \tag{17}$$

where $\tau = \frac{Q^2}{4m_p^2}$, ϵ_γ is the longitudinal virtual photon polarization, and the $\pm$ stands for the two possible orientations of the electron beam helicity.

For each Q^2, a single measurement of the azimuthal angular distribution of the proton scattered in a secondary target (described later) gives both the longitudinal and transverse polarizations. Combining Eq. 16 and 17 gives:

$$\frac{G_{Ep}}{G_{Mp}} = -\frac{P_t}{P_l} \frac{(E_e + E'_e)}{2M} \tan \frac{\theta_e}{2}, \tag{18}$$

thus the ratio of electric to magnetic form factors of the proton is obtained directly from a simultaneous measurement of the two recoil polarization components. The kinematic factors in Eq. 18 are typically known to a precision far greater than the statistical precision of the recoil polarization components.

4.1 Focal Plane Polarimetry

The azimuthal distribution of the protons which undergo a second scattering in the analyzer is dependent upon the proton polarization due to the spin-orbit part of the strong nuclear force [63]. The degree of polarization is directly related to the asymmetry of this angular distribution by:

$$N_p^{\pm}(\theta, \phi) = N_p^{\pm}(h=0) \Big[1 + (\pm h A_y(\theta) P_t^{fp} + a_i) \sin\phi + (\pm h A_y(\theta) P_l^{fp} + b_i) \cos\phi \Big], \tag{19}$$

where $N_p^{\pm}(h=0)$ is the number of protons incident on the polarimeter, h is the helicity, and a_i and b_i are the instrumental asymmetries. Empirically, the analyzing power, A_y, is the amplitude of the asymmetry resulting from the scattering of a particle with polarization, P_y, i.e. $A_y = \frac{A}{P_y}$. It is important to note that in this experiment to extract P_t^{fp} and P_l^{fp}, we take the **difference** in angular distributions of positive and negative electron helicities, and thus are completely insensitive to the instrumental asymmetries.

The crucial feature of the polarimeter is its coefficient of merit (COM), defined as:

$$COM = \int_{\vartheta_{min}}^{\vartheta_{max}} \epsilon(\vartheta) A_y(\vartheta) \sim \epsilon \bar{A}_y^2, \tag{20}$$

where $\epsilon(\vartheta)$ is the differential fraction of events scattered in the analyzer at polar angle ϑ, and $A_y(\vartheta)$ is the corresponding analyzing power. The data are binned in ϑ, and a value of $G_{Ep}/G_{Mp}(\vartheta)$ obtained for each bin; the weighted average is the result of the experiment.

4.2 Spin Precession

In all recoil polarization experiments, elastic ep events are identified by using coincidence detection of both electron and proton. In this experiment, the electron will be detected using the BigCal lead-glass detector array (as was the case in the completed Gep-III (JLab E04-108) experiment in Hall C), and the proton will be detected with the planned SuperHMS (SHMS) spectrometer. As the proton travels through the SHMS, its spin precesses due to the interaction of the magnetic moment of the proton with the magnetic elements of the SHMS, which consists of a horizontal bending magnet, followed by a series of quadrupole magnets as well as the principal vertical bend dipole magnet.

The proton polarization at the spectrometer focal plane is related to its polarization at the target by a spin matrix:

$$\begin{pmatrix} \mathbf{P_n^{fp}} \\ \mathbf{P_t^{fp}} \\ P_l^{fp} \end{pmatrix} = \begin{pmatrix} S_{nn} & \mathbf{S_{nt}} & \mathbf{S_{nl}} \\ S_{tn} & \mathbf{S_{tt}} & \mathbf{S_{tl}} \\ S_{ln} & S_{lt} & S_{ll} \end{pmatrix} \begin{pmatrix} P_n^{tar} \\ \mathbf{P_t^{tar}} \\ \mathbf{P_l^{tar}} \end{pmatrix}$$

The focal plane polarimeter measures only the transverse and normal, P_t^{fp} and P_n^{fp}, components of the proton polarization. The spin matrix is calculated using a model of the spectrometer with the differential-algebra-based transport code COSY. Details are given in Ref. [10] regarding the method for extracting the target polarizations from knowledge of the spin matrix and measurement of the $N(\theta, \phi)$ distributions. For a standard QQQD magnet spectrometer, the spin matrix components, S_{nt} and S_{tl}, are almost zero when averaged over the phase space. The addition of the horizontal bender in front of the SHMS QQQD magnet system creates a potential complication, since the phase space averaged S_{nt} and S_{tl} will now have a non-zero value.

The effect of the horizontal bending magnet is to mix the transverse and longitudinal components, P_t^{tar} and P_l^{tar} of the outgoing elastic proton. After the horizontal bender, the transverse and longitudinal components are

$$P_t^{hb} = P_l^{tar} \sin\phi_{hb} + P_t^{tar} \cos\phi_{hb}, \quad (21)$$

$$P_l^{hb} = P_l^{tar} \cos\phi_{hb} - P_t^{tar} \sin\phi_{hb}, \quad (22)$$

in which $\phi_{hb} = \kappa_p \gamma \theta_{bend}^H$ is the precession angle of the horizontal bending magnet. The bend angle of the magnet, θ_{bend}^H, is 3°. For Q^2 = 10.5 and 13 GeV^2, $\gamma = 7.0$ and 8.4 which gives ϕ_{hb} = 37.5° and 45.1°, respectively. For spin transport after the horizontal bender to the SHMS focal plane, we will ignore the quadrupoles and treat the dipole magnet as a simple dipole. Of course in the actual experiment, we will use the full calculation of the spin matrix, a technique which has been firmly established in the previous JLab experiments, and which is well understood.

The transverse and normal components, P_t^{fp} and P_n^{fp}, at the SHMS focal plane are

$$P_t^{fp} = P_t^{hb} = P_l^{tar} \sin\phi_{hb} + P_t^{tar} \cos\phi_{hb}, \quad (23)$$

$$P_n^{fp} = P_l^{hb} \sin\phi_d = (P_l^{tar} \cos\phi_{hb} - P_t^{tar} \sin\phi_{hb}) \sin\phi_d. \quad (24)$$

P_t^{hb} is unchanged by the simple dipole magnet and P_l^{hb} is rotated by the dipole's precession angle, $\phi_d = \kappa_p \gamma \theta_{bend}^D$. With the dipole's bend angle, θ_{bend}^D, equal to 18.4°, this gives $\phi_d =$

229.7° and 276.5°, at $Q^2 = 10.5\ GeV^2$ and $Q^2 = 13\ GeV^2$, respectively, which is in general very favourable for this experiment, especially at the largest Q^2 value considered.

For a simple estimate of the uncertainty on the target polarization components one rewrites the equations as:

$$P_t^{tar} = P_t^{fp}\cos\phi_{hb} - P_n^{fp}\frac{\sin\phi_{hb}}{\sin\phi_d} \quad (25)$$

$$P_l^{tar} = P_t^{fp}\sin\phi_{hb} + P_n^{fp}\frac{\cos\phi_{hb}}{\sin\phi_d} \quad (26)$$

The fractional uncertainty on P_t^{fp} and P_n^{fp} is $\sqrt{\frac{2}{NA^2}}$ where A is the analyzing power and N is the number of protons which scatter in the analyzer in a given angular range. Thus, the uncertainties on the target polarizations are

$$(\Delta P_t^{tar})^2 = (\Delta P_t^{fp})^2\cos^2\phi_{hb} + (\Delta P_n^{fp})^2\frac{\sin^2\phi_{hb}}{\sin^2\phi_d}, \quad (27)$$

$$(\Delta P_l^{tar})^2 = (\Delta P_t^{fp})^2\sin^2\phi_{hb} + (\Delta P_n^{fp})^2\frac{\cos^2\phi_{hb}}{\sin^2\phi_d}. \quad (28)$$

Since $\Delta P_t^{fp} = \Delta P_n^{fp} = \sqrt{\frac{2}{NA^2}}$, the equations can be rewritten as

$$(\Delta P_t^{tar})^2 = \frac{2}{NA^2}(\cos^2\phi_{hb} + \frac{\sin^2\phi_{hb}}{\sin^2\phi_d}) \quad (29)$$

$$(\Delta P_l^{tar})^2 = \frac{2}{NA^2}(\sin^2\phi_{hb} + \frac{\cos^2\phi_{hb}}{\sin^2\phi_d}) \quad (30)$$

For Q^2 = 13 GeV^2, $\sin\phi_d \approx 1$, and thus $\cos^2\phi_{hb} + \frac{\sin^2\phi_{hb}}{\sin^2\phi_d} \approx 1$ and the uncertainties on the target polarizations are approximately equal to those at the focal plane. For Q^2 = 10.5 GeV^2, $\sin\phi_d \approx 0.76$, the uncertainties on the target polarizations are multiplied by ≈ 1.30 for both ΔP_t^{tar} and ΔP_l^{tar}. Without the horizontal bending magnet only ΔP_l^{tar} would be increased by the precession in the dipole magnet.

5 The Experiment

This experiment will use the Super High Momentum Spectrometer (SHMS) in Hall C to detect the recoiling proton, and the BigCal lead glass calorimeter to detect the scattered electron. The focal plane in the SHMS will be equipped with the Focal Plane Polarimeter (FPP) that was installed in the HMS spectrometer in Hall C for the Gep-III experiment; indeed, the SHMS focal plane detector package has been designed to allow for the installation of the Hall C FPP. We have assumed the existence of a 30 cm long liquid hydrogen target, which of course can and will be used for a multitude of experiments in Hall C in the 12 GeV era. Therefore, this experiment requires no new equipment beyond the base equipment planned for the Hall C 12 GeV upgrade.

5.1 The Super High Momentum Spectrometer

The SHMS bends charged particles in both the horizontal and vertical plane; it consists of a horizontal 3° bending magnet, whose primary function is to allow access to small scattering angles, followed by three quadrupoles, and finally one vertical bend dipole magnet. Its angular acceptance is approximately 5.0 msr. The angular resolution is approximately 1.2 mr in both the in-plane and out-of-plane directions, and the momentum resolution is approximately 0.03-0.08%. These momentum and angular resolutions are perfectly adequate for this experiment. The highest momentum accepted by the SHMS is 10.4 GeV/c, corresponding to Q^2=18 GeV^2; the vertical bend angle of the SHMS is 18.4°.

As described in the previous section, favorable precession angles are crucial to obtain the ratio G_{Ep}/G_{Mp} with small uncertainty. For the Q^2 range considered in this experiment (10 GeV^2 $< Q^2 <$ 14 GeV^2), the precession angles are very favourable.

5.2 The Focal Plane Polarimeter

This experiment requires the installation of a Focal Plane Polarimeter (FPP) in the focal plane area of the SHMS. As shown in Fig. 13, the design of the focal plane detection system for the SHMS has been planned from the beginning to be able to incorporate the FPP which was installed in the HMS in Hall C and used successfully for the Gep-III experiment. The analyzer of the FPP is divided into two blocks of CH_2, each 55 cm thick. The incoming proton trajectories will be reconstructed from using the SHMS focal plane drift chambers. Outgoing trajectories of scattered particles in either of the two analyzers are reconstructed using the FPP drift chambers. This is the same algorithm that has been implemented with the FPP in the HMS during Gep-III; thus, the migration of our analysis software should be straightforward.

The FPP has been designed as a unit in a sturdy frame, to facilitate its installation and removal. It will be required for this experiment that a basic underlying structure be built to support the FPP frame itself within the SHMS detector hut, just as has been done for the FPP in the HMS.

For the purposes of determining the polarimeter COM for calculating projected uncertainties, the differential scattering fraction has been estimated from a full Geant3-based simulation of the polarimeter. Results obtained for the scattering fraction from this simulation are in good agreement with the results of previous experiments (as well as, most importantly, with recent results from Gep-III), and thus we are confident in our estimates for this new experiment. In Fig. 14, we show the currently available maximum analyzing power data from the previous JLab experiments, including our most recent results from Gep-III, as well as from measurements at Dubna[64] for CH_2, and at Saclay[65] and Moscow[66] for carbon. A combined analysis[64] of the carbon and CH_2 data showed that empirically, the maximum analyzing power is proportional to $1/p$ over a large range of momenta. Moreover, the shape of the analyzing power curve as a function of transverse momentum (which is proportional to the polar angle, ϑ) is largely independent of momentum, as well, with the analyzing power reaching a maximum value at $p_t \simeq 0.3$ GeV/c. We have extrapolated the linear fit to the data into the region of proton momenta which correspond to this experiment, and have used these values to estimate the average analyzing powers.

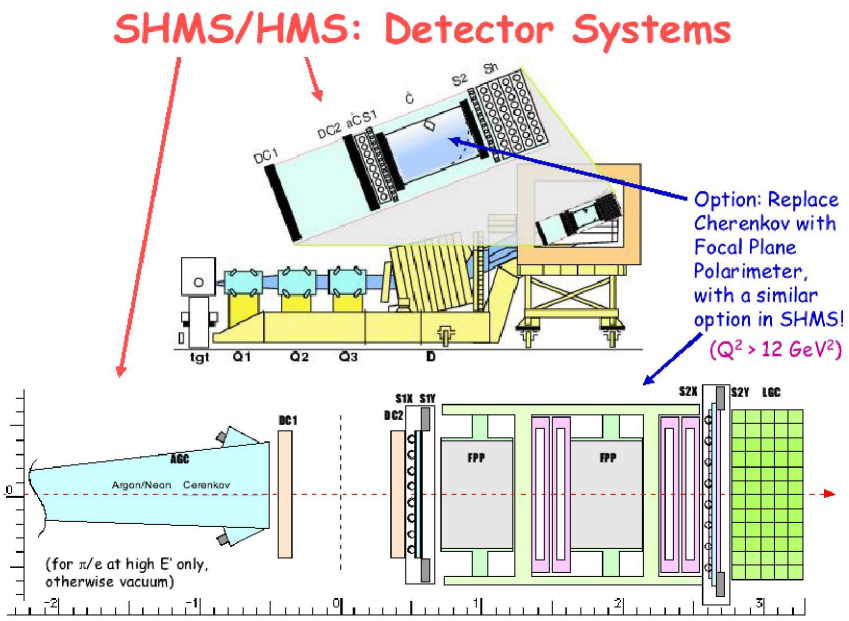

Figure 13: *Schematic Drawing of the planned SHMS focal plane detection package.*

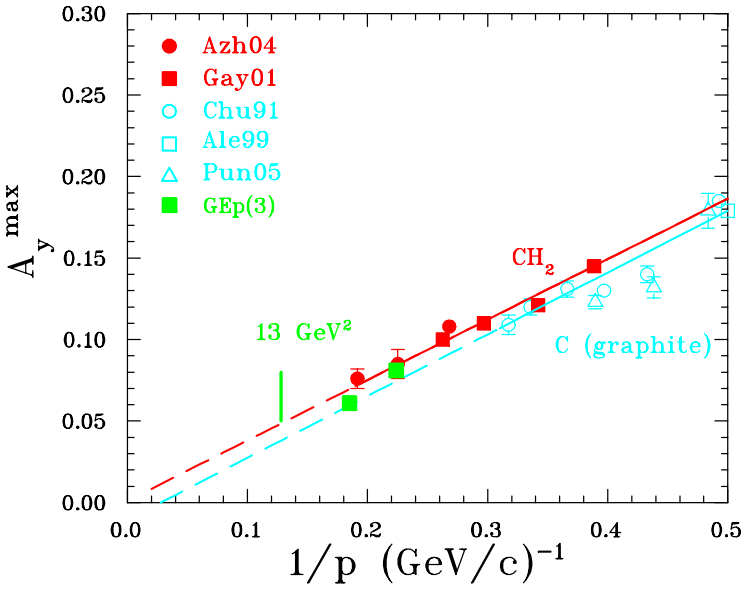

Figure 14: *Maximum carbon/CH_2 analyzing power data.*

Figure 15: *The BigCal Calorimeter.*

5.3 BigCal Calorimeter

Essential to this experiment is solid angle matching, which means that for each kinematics the solid angle of the electron detector must match the fixed solid angle of the proton detector, which is the SHMS. With a beam energy of 8.8-11.0 GeV, the kinematics of this experiment are such that the electron scattering angle is larger than the proton recoil angle, and therefore the Jacobian for the electron is larger than 1, and hence the solid angle for the electron detector must be larger than that of the proton detector.

Of course, the situation here is exactly the same as for the Gep-III experiment in Hall C, for which a new large lead glass calorimeter array (BigCal) was constructed (See Fig. 15). This is the ideal detector for the electron in this experiment as well, as no modifications will be necessary.

BigCal consists of 32 columns times 32 rows of 3.8×3.8 cm^2 bars of Protvino lead glass blocks at the bottom, and 30 columns times 24 rows of 4.0×4.0 cm^2 from RCS (Yerevan blocks) placed on the top. The total frontal area is thus 2.63 m^2. At a distance of 10.0 m away from the target, the detector offers a solid angle of 26 msr to the electrons of the ep

reaction, which is adequate for all of the kinematics of this experiment. The pulse height from every lead glass bar is digitized. In addition, after splitting in the multiplexer/amplifier circuit, a copy of the original signal is added in groups of eight channels for timing purposes, as well as for constructing the calorimeter trigger. The timing information helps distinguish noise from true charge sharing. Interpolation over the charge sharing in neighboring bars is expected to improve the position resolution from the canonical d/$\sqrt{12}$ $\sim$1.2 cm, where d is the bar's transverse size. A preliminary analysis of data from the Gep-III experiment results in a position resolution of approximately 8 mm at an electron energy of 2.35 GeV. Assuming that the position resolution scales as $1/\sqrt{E}$, we would predict a position resolution of 6-7 mm at the energies involved in this experiment. At a 10 m distance from the target, this corresponds to an angular resolution of approximately 0.6 mr; this is better than is needed for this experiment, given the projected angular resolution of the SHMS ($\sim$ 1.2 mr) together with the large value of Jacobian for the planned kinematics.

5.3.1 Radiation Hardness of BigCal

BigCal was used in experiments 04-019 (Gep2γ), 07-002 (WACS) and 04-108 (Gep-III) in Hall C between October 2007 and June 2008. Before the experiments, BigCal was roughly calibrated with cosmic muons. The first task with beam was commissioning BigCal using 1.06 GeV elastic electrons. To reduce the radiation damage, BigCal has an absorber consisting of four removable aluminum 1-inch thick plates in front of the lead glass. In addition, a lucite plate (for checking the lead glass PMTs with an LED system) and a 1/2 inch aluminum plate are permanently placed in front of the lead glass. Two absorber configurations were used during the calibration. The first used only one of the removable aluminum plates, and the second used all four plates, which together with the permanent aluminum plate results in thicknesses of 0.43 X_0 and 1.29 X_0 respectively. In Fig. 5.3.1, the measured energy resolutions are plotted as filled red squares at their given aluminum thickness. Also plotted in Fig. 5.3.1 are the predicted energy resolutions at different incident electron energies and aluminum thicknesses from a GEANT Monte Carlo simulation [68]. The experimentally achieved energy resolution differs by about 1-1.5% from the simulations and is among the best results obtained with this type of calorimeter especially given the additional absorber and the large number of channels.

During E04-019 and Gep-III,which both measured the elastic ep reaction, the PMT gains in BigCal could be continually monitored using the predicted electron energy calculated from the measured angle and momentum of the proton detected in the HMS. Depending on the kinematics, the experiment could collect enough data in 1 to 8 hours to do a calibration. Due to the darkening of the lead-glass from radiation damage, there was an effective drop in the PMT gain and the energy resolution in BigCal gradually decreased (i.e. increased width) thoughout the experiments. Most of the time, the PMT gain shifts were corrected in software, but when the shifts became large enough the HV of the PMTs was adjusted to increase the gain. By the end of the experiments the energy resolution was 24%/$\sqrt{(E)}$, despite doing a partial UV curing of BigCal in January 2008 in the middle of the experiments. Fig. 5.3.1 is a plot of the relative PMT gain versus the accumulated charge throughout all of the experiments. The relative gain, normalized to one at the beginning of the experiments, was obtained by averaging the gain of all the channels. For the relative gains shown in Fig. 5.3.1, when adjustments of the PMT HV were made the new gain was normalized to

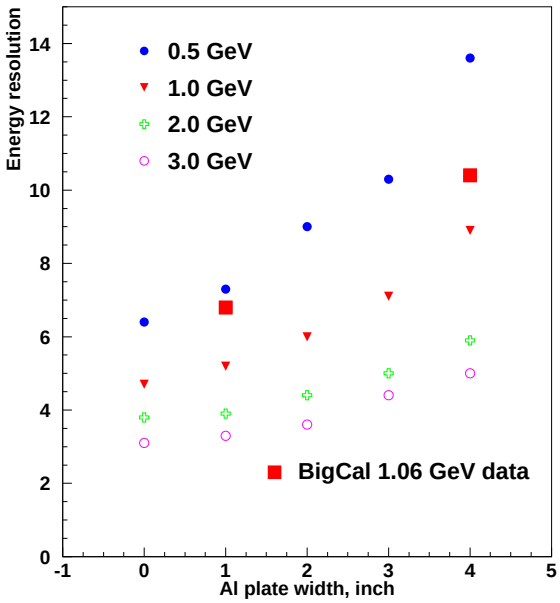

Figure 16: *BigCal energy resolution (red solid boxes) obtained during commissioning using 1.06 GeV elastic electrons with two different absorber thicknesses (total thicknesses of 0.43 X_0 and 1.29 X_0, respectively) compared to Monte Carlo simulations for different energies as function of the additional Al absorber thickness.*

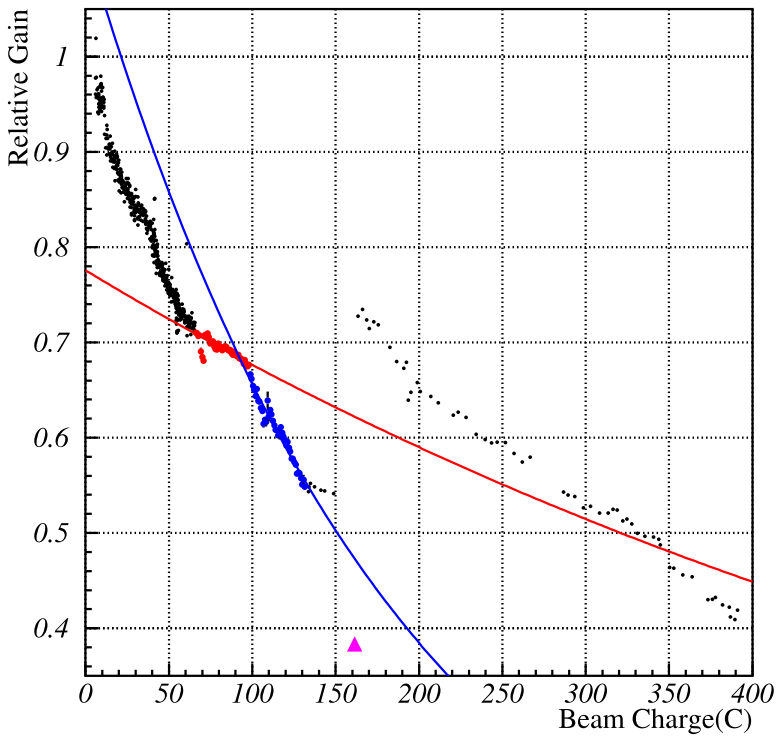

Figure 17: *Mean gain of BigCal during the Gep-III experiments in Hall C (October 2007 - June 2008) as a function the accumulated beam charge in coulombs. The red (blue) points are during E04-019 with BigCal at angle of 44.9° (32°). The data points are fitted with* ae^{-bC} *(results given in Table 5.3.1). No data for the week-long WACS experiment (E07-002) is given except the last run (solid magenta triangle) just before the UV curing.*

the previous value so that effective gain comparison can be done relative to the initial high voltages. A number of BigCal configuration changes were done during these experiments. For each new configuration, the effective gain of the PMTs would change (mainly due to dependence of the energy loss in the absorber on the electron energy) and a correction was applied at the beginning of each kinematics to ensure the continuity of the gain before and after the change of the kinematics. Generally, the different slopes in Fig. 5.3.1 correspond to different kinematics: different beam energy, angle and distance to the calorimeter.

After the E04-019 kinematics point with BigCal at 32° (blue points in Fig. 5.3.1), the Wide Angle Compton Scattering (WACS) experiment started. WACS used a 6% radiator in front of a 15cm target liquid hydrogen target with BigCal placed at 12 m distance and an angle of 27°. Since normal WACS running did not have elastic ep events, the gain could not be monitored continuously. Only at the end of WACS were data taken for elastic ep events. The calibration point is the solid magenta triangle in Fig. 5.3.1 which shows a steep decline in the BigCal gain during the WACS experiment due to the forward BigCal angle and the radiator at the target.

After WACS the beam was down for a one month period, so it was decided to restore the lead glass by using UV curing. Curing of the glass was performed with a specially constructed UV lamp that covered a quarter of the frontal calorimeter area. The lamp was

Experiment	angle deg.	Dist. m	Target Length cm	Beam Energy GeV	Gain loss rate b	soft photon flux J/cm^2/C
E04-019	44.9	12	20	2.839	0.14 %/C	0.0039
E04-019	32.0	11.2	20	3.539	0.53 %/C	0.013
Gep-IV (Q^2 = 6)	30.0	10	30	6.6	1.11 %/C	
Gep-IV (Q^2 = 10.5)	35.5	10	30	8.8	0.80 %/C	
Gep-IV (Q^2 = 13)	31.3	10	30	11.0	1.04 %/C	

Table 1: *Gain loss per coulomb of beam estimated from the Fig. 5.3.1 for E04-019 at two angles. The GEANT prediction for the soft photon flux per coulumb for the two E04-019 points. For each Gep-IV, the gain loss per coulomb is estimated by interpolating between E04-019 points and scaling for the increased target thickness.*

moved at four different positions with an average time of 3 days per position. The effect of the UV curing corresponds to the jump in Fig. 5.3.1 between the red triangle (at 39%) indicating the gain before the curing and the next upper point (at 74%) after the curing. Fit with exponential function gives 1.24% per hour gain increase. Because of concerns about glass heating, there was a gap of 2" between the UV bulbs and the glass. During the curing it turned out that the glass temperature rose by a few degrees, so the UV lamps could have be placed closer to the glass. Low power bulbs (14W) were used so that damage the PMTs that were left in place during the curing did not occur. After the Gep-III experiment, an additional UV lamp was built so that two UV lamps were available to cure the calorimeter for the SANE experiment with expected total curing time of 60 days per position. Constant check of the PMT performance showed no deviation from the normal gain, except some relaxation time was needed after long (several weeks) period of UV illumination.

The BigCal positions for this proposed experiment will be between 30.0° to 35.5° and at 10 m from the target. To estimate the gain loss due to radiation damage to BigCal in this proposed experiment, two kinematic settings from E04-019 that had BigCal at 32° and 44.9° were studied. Both settings placed BigCal at about 11-12 m from the target. As shown in Fig. 5.3.1, the data points were fitted with the form: ae^{-bC} and the rate constant b is given in Table 5.3.1. Using GEANT simulations, the energy fluxes per coulumb through the front of the calorimeter have been estimated for the both settings. As seen in Table 5.3.1, these numbers are roughly proportional to the gain loss rates estimated from Fig. 5.3.1. Thus, for the Gep-IV kinematics, one can predict the gain loss by assuming that it changes linearly with angle and target length. Also, it was assumed that the gain loss scaled as the square of the BigCal distance from the target. The predicted gain loss per Coulomb is given in Table 5.3.1. With 75uA current and 50% running efficiency, one expects 3.25 C /day which means a 3.4% drop in gain per day for the Q^2 = 13 point. Given the length of the experiment, a UV curing of the lead-glass will be needed on average once a week (about 24% drop in gain) during the experiment.

We intend to built a permanent UV light box in front of the glass. By placing the bulbs right next to the glass and increasing the power and density of the bulbs we expect to increase the UV flux by at least 5 times resulting in a gain increase rate of above 6%/hour. This means in 4 hours about one weeks worth of damage to the lead glass could be cured. The curing

of the lead glass could be done during normal beam maintanence down times which happen every week, so that the experiment has no loss in efficiency.

5.3.2 A Possible Alternative to BigCal - Upgraded HYCAL

Interest in a general purpose radiation-hard medium-sized calorimeter that could be used in multiple experiments has been building at Jefferson Lab. A hybrid calorimeter, HYCAL, was used in the Hall B PrimEx I experiment and will be used in the follow-up PRIMEX II experiment currently planned for 2012 in Hall B. HYCAL consists of an inner section of 1052 $PBW0_4$ scintillating crystals surrounded by 576 lead glass bars which is arranged in a 1.18x1.18 m^2 grouping. The PrimEx I experiment measured the position resolution of the $PBW0_4$ section to be approximately 2 mm. Also, $PBW0_4$ is known to be about 100 times more resistant to radiation damage than lead glass. For our proposed experiment, however, the current incarnation of HYCAL is not a good alternative to BigCal. With HYCAL's smaller size, it would have to be located at a distance of 5 m from the target, and so the lead-glass section of HYCAL would receive significantly worse radiation damage problems than BigCal.

A Hall D proposal, "A Precision Measurement of the η Radiative Decay Width via the Primakoff Effect", plans to use HYCAL, but also suggests the possibility of upgrading HYCAL by replacing the lead-glass part of the detector with $PBW0_4$ bars and having the same 1.18x1.18 m^2 size. This new detector would be for general purpose use in other halls. This detector could be used in our proposed experiment. The detector would be placed approximately 5 m away from the target. The upgraded HYCAL could be placed at 33° and would be able to cover all three Q^2 points without moving HYCAL. With a 2 mm position resolution, the electron angular resolution would be 0.4 mr which is better than expected with the BigCal at 10m. Given that the $PBW0_4$ suffers less radiation damage by a factor of 100, the radiation of the $PBW0_4$ should only reduce the gain by about 8% over the course of the experiment. This means that UV curing during the experiment would not be needed.

5.4 Measurements

In Tab. 2, we present a summary of the kinematic points that have been chosen. In the appendix, we include further discussion of the various kinematic choices that were also evaluated. There are several features that are worth noting:

- At a Q^2 value of 6 GeV^2, the electron scattering angle is approximately the same as for the Q^2=13 GeV^2 point. Thus, this control point could be taken in a short amount of time, and it does not require that the calorimeter be moved to a third position in Hall C.

- While in principle all kinematics considered here can be reached using a beam energy of 8.8 GeV, beyond $Q^2 \sim 12$ GeV^2, electron solid angle matching considerations as well as the overall cross section dependence with energy favour a 11.0 GeV beam energy.

In Fig. 18, we show the predicted angular acceptance of the SHMS including the horizontal bending magnet. Not surpisingly, the out-of-plane acceptance is about a factor of

Q^2	E_e	θ_e	$E_{e'}$	θ_p	p_p	$d\sigma/d\Omega_e$	ϵ	χ	$\Delta\Omega_e$
GeV^2	GeV	deg	GeV	deg	GeV/c	cm^2/sr		deg	msr
6	6.6	30	3.4	25	4.03	1.1×10^{-35}	0.72	145.4	8.6
10.5	8.8	35.5	3.20	16.7	6.47	3.5×10^{-37}	0.55	229.7	24
13	11.0	31.3	4.07	15.7	7.81	1.6×10^{-37}	0.58	276.5	23

Table 2: *The proposed kinematics. Assumed SHMS spectrometer solid angle: 5 msr. Assumed beam characteristics: 75 μA, 85% polarization. Assumed target: 30 cm LH_2.*

Q^2	$\Delta\theta_e$	$\Delta\phi_e$	Δy	Δx
GeV^2	mr	mr	m	m
6	$\pm$ 32.7	$\pm$ 65.4	0.809	1.310
10.5	$\pm$ 55.1	$\pm$ 110.0	1.287	2.209
13	$\pm$ 53.4	$\pm$ 107.0	1.233	2.148

Table 3: *Size Requirements for the Electron Detector. Assumed distance from target: 10 m. Assumed target: 30 cm LH_2.*

two larger than the in-plane acceptance. This is similar (in aspect ratio) to the HMS angular acceptance, and hence the current configuration of BigCal, which was optimized to match the HMS acceptance and using a similar length LH_2 target, is ideal for this experiment as well. In Tab. 3, we give the projected horizontal (y) and vertical (x) size requirements for the electron detector for the three kinematics points that have been chosen.

Of particular importance in this experiment, as well as in Gep-III, is our ability to cleanly identify elastic $e-p$ scattering events; indeed, the fraction of elastic events compared to inelastic and other background events continues to decrease with increasing momentum transfer. As evidence of the effectiveness of the algorithm for identifying elastic events, we show in Fig. 19 data from Gep-III at $Q^2 = 6.8\ GeV^2$ and $Q^2 = 8.5\ GeV^2$. The plots are histograms of the proton mome ntum as measured by the HMS spectrometer. The red curve is for all events. The cyan curve results after applying a cut corresponding to the expected δ vs. θ_p correlation for elastically scattered protons. The magenta curve corresponds to those events which also pass a coplanarity cut between the scattered electron (as measured in BigCal) and the scattered proton. Finally, the green curve results from a cut on the expected position of the electron in BigCal, together with a cut on expected correlation in the polar scattering angles of the electron and proton. We estimate that the background contamination from non-elastic events after the application of these cuts is less than 1%. In addition, as the SHMS momentum and angular resolution are similar to those of the HMS, we anticipate that similar results can be acheived in the Gep-IV experiment, as well.

In Tab. 4, we show projected uncertainties and beam times for all of the kinematics considered. In our opinion, the 120 days of beam time required to acquire a data point at Q^2=14 GeV^2 (see Appendix) eliminates this from consideration at this time. At the same time, extending these measurements to the highest reasonable Q^2 value possible strongly motivates using the SHMS spectrometer to make a measurement at Q^2=13 GeV^2. As the focal plane polarimeter must be relocated to the SHMS for this measurement, then logistics dictate that

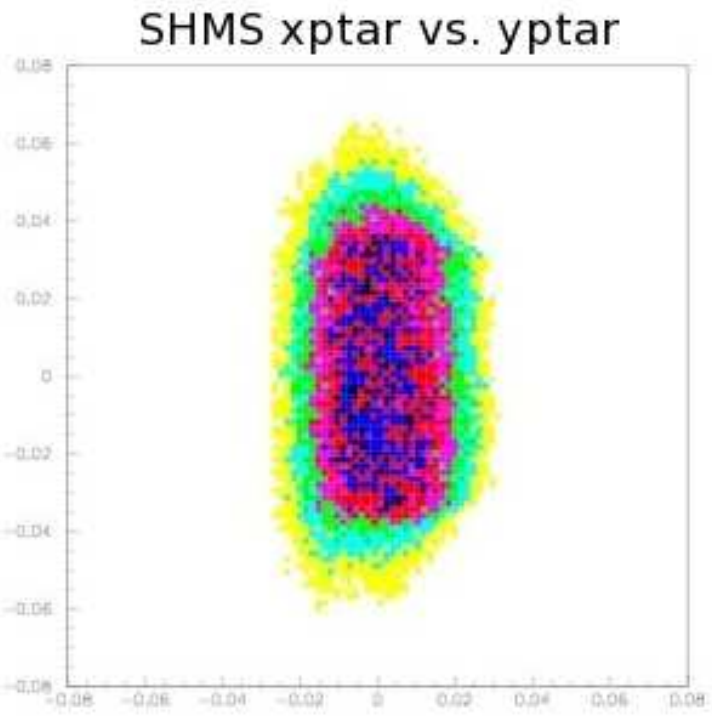

Figure 18: *Monte Carlo Simulation of SHMS Angular Acceptance.*

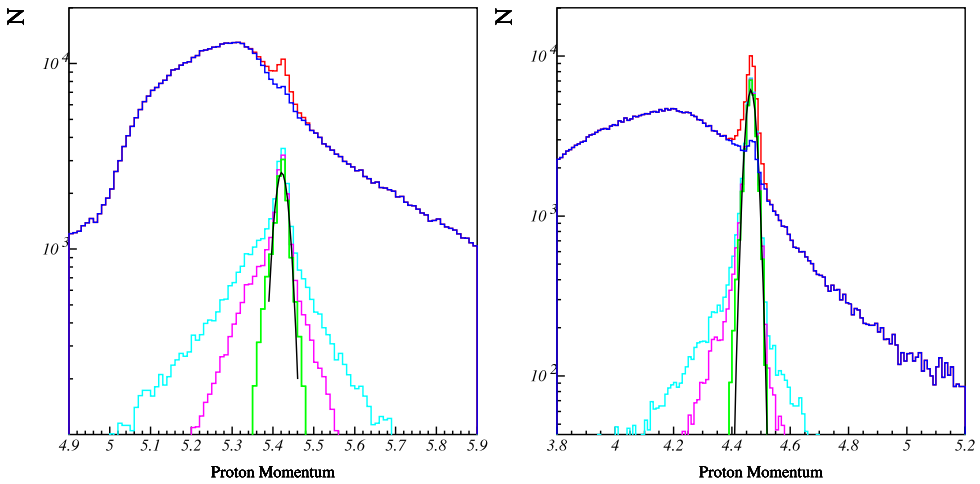

Figure 19: *Identification of Elastic ep Scattering Events in the Gep-III Experiment. The left panel shows data from taken at $Q^2 = 8.5\ GeV^2$ and the right panel shows the $Q^2 = 6.8\ GeV^2$ data. The various curves are explained in the text. In each figure, the green curve represents the strictest set of cuts, and results in a non-elastic background contimination of less than 1%.*

Q^2	E_e	COM	absolute $\Delta(G_{Ep}/G_{Mp})^*$	time
GeV^2	GeV			days
6.0	**6.6**	**3.9×10^{-3}**	**0.04**	**4**
10.5	**8.8**	**1.5×10^{-3}**	**0.11**	**30**
13.0	**11.0**	**1.1×10^{-3}**	**0.13**	**60**

Table 4: *Absolute uncertainties (not including systematics), and times required. The assumed beam intensity and electron beam polarization are 75 μA and 0.85, respectively. The target length is 30 cm, and the SHMS solid angle is 5.0 msr.*
* *Note that the increase in the error bar due to precession in the horizontal bender has already been included in this estimate. See the Appendix for further details.*

we carry out all measurements using the SHMS. Considering that Gep-III has measured a point at Q^2=8.5 GeV^2, we opt for an additional point in this experiment at Q^2=10.5 GeV^2, which essentially is half way between the Gep-III data point and our highest Q^2 data point. In addition, a control point at Q^2=6 GeV^2, requiring only 4 days of beam time, seems very reasonable.

6 Summary

The total beam time requested for these three new data points is approximately 94 days. In Fig. 20, we summarize the currently available data for the proton form factor ratio, together with preliminary data from Gep-III, and the projected error bars for the approved E12-97-112 experiment in Hall A, and of course for this experiment. We alo include the current projections from a range of theoretical models. In addition to the models discussed previously, we also show two phenomenological Vector Meson Dominance (VMD) inspired calculations, one by Lomon [67], and another by Bijker and Iachello [19]. It seems clear that data from the experiment will provide severe constraints on these and other models of this fundamental quantity.

We close by quoting the authors of the pCDR document for the 12 GeV JLab upgrade:

> "The JLab 12 GeV Upgrade will support a great leap forward in our knowledge of hadron structure through major programs in three areas: nucleon form factors at large Q^2, valence quark structure, and deep exclusive scattering."

We feel that the proposed experiment represents an opportunity which is in fact unique in the world to provide data on the proton form factor ratio at large Q^2, an essential ingredient in our understanding of the internal structure of hadrons.

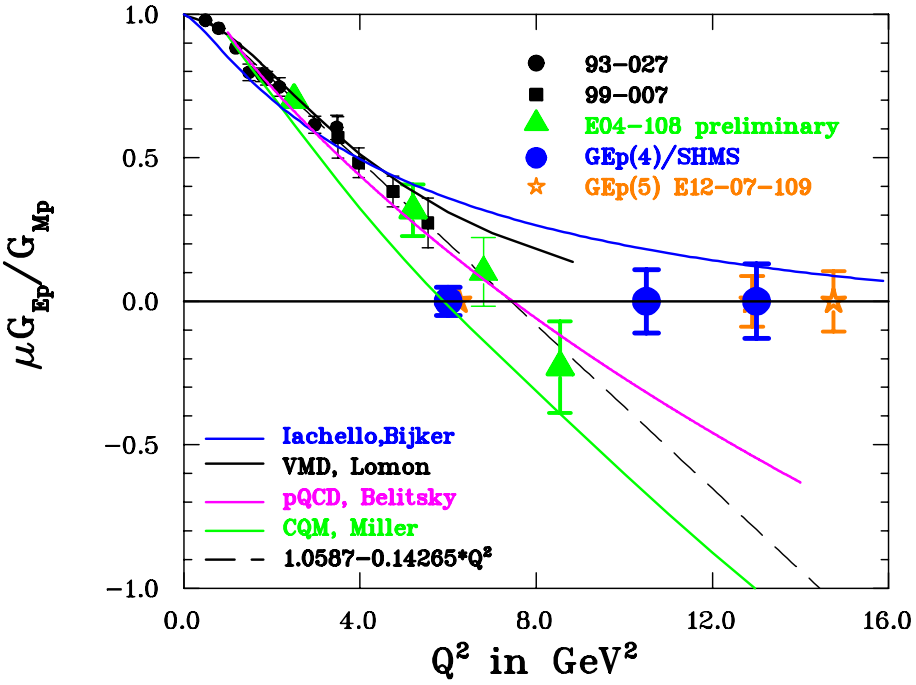

Figure 20: *The new data points proposed here, versus the projected results of E12-07-109, the preliminary results from Gep-III and the older recoil polarization database. A selection of recent model calculations is also shown.*

Q^2	E_e	θ_e	$E_{e'}$	θ_p	p_p	$d\sigma/d\Omega_e$	ϵ	χ	$\Delta\Omega_e$
GeV^2	GeV	deg	GeV	deg	GeV/c	cm^2/sr		deg	msr
6.0	6.6	30	3.4	25	4.03	1.1×10^{-35}	0.72	145.4	8.6
9.0	8.8	29.3	4.00	20.5	5.66	1.4×10^{-36}	0.67	201.6	12
10.5	8.8	35.5	3.20	16.7	6.47	3.5×10^{-37}	0.55	229.7	24
12	8.8	44.2	2.77	13.3	7.27	0.85×10^{-37}	0.27	259.0	353
12	11.0	28.2	4.61	17.4	7.27	3.3×10^{-37}	0.64	259.0	15
13	11.0	31.3	4.07	15.7	7.81	1.6×10^{-37}	0.58	276.5	24
14	8.8	66.0	1.34	12.1	8.35	0.1×10^{-37}	0.19	295.3	224
14	11.0	34.9	3.54	14.0	8.35	0.7×10^{-37}	0.50	295.3	33

Table 5: *The proposed kinematics. Assumed SHMS spectrometer solid angle: 5.0 msr. Assumed beam characteristics: 75 μA, 85% polarization. Assumed target: 30 cm LH_2.*

Q^2	E_e	COM	Horiz. Bender	$\Delta(G_{Ep}/G_{Mp})^*$	time
GeV^2	GeV		Factor		days
6.0	**6.6**	**3.9×10^{-3}**	**1.15**	**0.04**	**4**
9.0	8.8	2.0×10^{-3}	1.70	0.11	30
10.5	**8.8**	**1.5×10^{-3}**	**1.30**	**0.11**	**30**
12.0	8.8	1.2×10^{-3}	1.01	0.12	60
12.0	11.0	1.2×10^{-3}	1.01	0.12	60
13.0	**11.0**	**1.1×10^{-3}**	**1.00**	**0.13**	**60**
14.0	8.8	0.9×10^{-3}	1.06	0.20	120
14.0	11.0	0.9×10^{-3}	1.06	0.16	120

Table 6: *Absolute uncertainties (not including systematics), and times required. The assumed beam intensity and electron beam polarization are 75 μA and 0.85, respectively. The target length is 30 cm, and the SHMS solid angle is 5.0 msr.*
* *Note that the increase in the error bar due to precession in the horizontal bender has been included.*

7 Appendix

In the process of evaluating the merits of various kinematic arrangements for this experiment, an array of choices were considered. In Tab. 5, we present a summary of the possible kinematic points that have been considered. Of course, using the existing HMS spectrometer to detect the recoil proton was certainly a reasonable option to consider, and in fact we have done so. However, we note that the largest value of Q^2 which can be reached with the HMS is 12 GeV^2. The limiting factor is of course the maximum momentum of the spectrometer. It is also important to note that in these kinematics, the spin precession (χ=350°) is not favourable. Therefore, we conclude that the SHMS is the only viable spectrometer in Hall C for these measurements.

In Tab. 6, we show projected uncertainties and beam times for all of the kinematics considered, along with the FPP coefficient of merit.

References

[1] M. Göeckler *et al.*, Phys. Rev. D **71**, 034508 (2005).

[2] C. Alexandrou, G. Koutsou, J.W. Negele, and A. Tsapalis, [arXiv: hep-lat/0605017], May 2006.

[3] R.C. Walker *et al.*, Phys. Rev. D **49**, 5671 (1994).

[4] L. Andivahis *et al.*, Phys. Rev. D **50**, 5491 (1994).

[5] M.E. Christy *et al.*, Phys. Rev. C **70**, 015206 (2004).

[6] I. A. Qattan *et al.*, Phys. Rev. Lett. **94**, 142301 (2005).

[7] M.K. Jones *et al.*, Phys. Rev. Lett. **84**, 1398 (2000).

[8] O. Gayou *et al.*, Phys. Rev. Lett. **88**, 092301 (2002).

[9] O. Gayou *et al.*, Phys. Rev. C **64**, 038202 (2001).

[10] V. Punjabi *et al.* Phys. Rev. C**71** (2005) 055202.

[11] A.V. Afanasev, *et al*, Phys. Rev. D**71**, 013008 (2005).

[12] P.G. Blunden, W. Melnitchouk, J.A. Tjon, P.R.L. **91** 142304 (2003).

[13] Y. M. Bystritskiy, E. A. Kuraev, and E. Tomasi-Gustafsson, Phys. Rev. C **75**, 015207 (2007).

[14] D. Borisyuk and A. Kobushkin, Phys. Rev. C **78**, 025208 (2008)

[15] E. Brash, M. Jones, C.F. Perdrisat, V.'Punjabi, E-04-108 "Measurement of GEp/GMp to 9 GeV^2 via recoil polarization" (2004).

[16] R. Gilman, L. Pentchev, C.F. Perdrisat, V. Punjabi, E-04-019 "Measurement of the Two-Photon Exchange Contribution in ep Elastic Scattering Using Recoil Polarization" (2004).

[17] J. Arrington, proposal E-05-017, "A measurement of two-photon exchange in unpolarized elastic electron-proton scattering" (2005).

[18] C.F. Perdrisat, V. Punjabi, M. Vanderhaeghen, Prog. in Part. Nucl. Phys. **59**, 694 (2007); arXiv:hep-ph/0612014.

[19] F. Iachello, A.D. Jackson, and A. Landé, Phys. Lett. **B43**, 191 (1973).

[20] M.F. Gari and W. Kruempelmann, Z. Phys. **A322**, 689 (1985) 689; M.F. Gari and W. Kruempelmann, Phys. Lett. **B274**, 159 (1992); M.F. Gari and W. Kruempelmann, Phys. Lett. **B282**, 483(E) (1992).

[21] S.J. Brodsky, G.R. Farrar, Phys. Rev. D 11 (1975) 1309.

[22] E.L. Lomon, arXiv nucl-th/0609020 (2006)

[23] R. Bijker and F. Iachello, Phys. Rev. **C69**, 068201 (2004).

[24] G. Höhler *et al*, Nucl. Phys. **B114**, 505 (1976).

[25] P. Mergell, U.G. Meissner, and D. Drechsel, Nucl. Phys. **A596**, 367 (1996).

[26] H.W. Hammer, , U.G. Meissner, and D. Drechsel, Phys. Lett. B**385**, 343 (1996).

[27] H.-W. Hammer and Ulf-G. Meissner, Eur. Phys. J. **A20**, 469 (2004).

[28] M.A. Belushkin, H.W. Hammer and U.G. Meissner, **C75**, 035202 (2007).

[29] J. Lachniet*et al*, arXiv:0811-1716 [nucl-ex] (2008).

[30] A. De Rujula, H. Georgi and S.L. Glashow, Phys. Rev. D **12**, 147 (1975); N. Isgur and G. Karl, Phys. Rev. D **18**, 4187 (1978); **19**, 2653 (1979); **20**, 1191 (1979); C. Hayne and N. Isgur, *ibid* **25**, 1944 (1982).

[31] P.L. Chung and F. Coester, Phys. Rev. D **44**, 229 (1991).

[32] M.R. Frank, B.K. Jennings and G.A. Miller, Phys. Rev. C **54**, 920 (1996).

[33] F. Schlumpf, Phys. Rev. D **47**, 4114 (1993).

[34] F. Cardarelli and S. Simula Phys. Rev. C **62**, 65201 (2000).

[35] E. Pace, G. Salme, F. Cardarelli and S. Simula, Nucl. Phys. A **666**&**667**, 33c (2000).

[36] M. De Sanctis, M.M. Giannini, L. Repetto and E. Santopinto, Phys. Rev. C **62**, 25208 (2000).

[37] S. Boffi *et al.*, Eur. Phys. J. A **14**, 17 (2002); S. Boffi *et al.*, hep-ph/0108271 v1 (2001).

[38] G.A. Miller, Phys. Rev. C **68**, 022201(R) (2003).

[39] Franz Gross and Peter Agbakpe, Phys. Rev. C **73**, 015203 (2006).

[40] A. Kvinikhidze and G.A. Miller, Phys. Rev. C **73**, 065203 (2006).

[41] F. Gross, G. Ramalho and M.T. Peňa, Phys. Rev. **77**:035203 (2008); arXiv:nucl-th/0606029 (2006).

[42] J.P.B. de Melo, T. Frederico, E. Pace,S. Pisano and G. Salme, arXiv:0804.1511 [hep-ph]

[43] S.J. Brodsky, hep-ph/0208158 v1 (2002).

[44] A.V. Belitzky, X. Ji and F. Yuan, hep-ph/0212351 (2003).

[45] J.P. Ralston and P. Jain, Phys. Rev.D **D69**, 053008 (2004).

[46] G.A. Miller and M.R. Frank, Phys. Rev. C **65**, 065205 (2002).

[47] A. Radyushkin, Phys. Rev. D **58**, 114008 (1998)

[48] A. V. Afanasev, arXiv:hep-ph/9910565.

[49] M. Guidal, M. V. Polyakov, A. V. Radyushkin and M. Vanderhaeghen, Phys. Rev. D **72**,054013 (2005).

[50] M. Diehl, T. Feldmann, R. Jakob and P. Kroll, Eur. Phys. J. C **39**, 1 (2005) [arXiv:hep-ph/0408173].

[51] M. Burkardt, Int. J. Mod. Phys. A**18**, 173 (2003)

[52] X. D. Ji, Phys. Rev. Lett. **78**, 610 (1997), Phys. Rev. D **55**,7114 (1997).

[53] J.J. Kelly, Phys. Rev. C **66**, 065203 (2002).

[54] G.A. Miller, Phys. Rev.Lett. **99**:112001 (2007); G.A. Miller and J. Arrington, Phys. Rev. C **78**:032201 (2008).

[55] K.J.Wilson Phys. Rev. D **10** (1974) 2445.

[56] C. Bernard *et al*, Phys. Rev. D **61**, (2000) 111502R, K. Orginos *et al*, Phys. Rev. **60** (1999) 054503.

[57] F. Farchioni *et al*, arXiv:hep-lat/0512017.

[58] R.G. Edwards *et al*, LHPC collaboration, arXiv:hep-lat/0610118.

[59] H.H. Matevosyan, G.A. Miller, and A.W. Thomas, Phys. Rev. C **71**, 055204 (2005).

[60] G. A. Miller, Phys. Rev. C **66**:032201 (2003).

[61] I.C. Cloët and C.D. Roberts, Proceed. of Sc. arXiv:0811.2018 [nucl-th] (2008); I.C. Cloët, G. Eichmann, B. El-Bennich, T. Klähn, and C.D. Roberts, arXiv:0812.0416 [nucl-th] (2008).

[62] A.I. Akhiezer and M.P. Rekalo, Sov. J. Part. Nucl. **3**, 277 (1974).

[63] E. Aprile-Giboni *et al*, NIM **215**, 147 (1943).

[64] L.S. Azhgirey *et al*., NIM A 538, 431 (2005).

[65] N.E. Cheung *et al*., NIM A 363, 561 (1995).

[66] I.G. Alekseev *et al*., NIM A 434, 254 (1999).

[67] E.L. Lomon, Phys.Rev. C **64**, 035204 (2001).

[68] Monte Carlo calorimeter simulations, including Cherenkov photon propagagtion through lead-glass, developed by K. Shestermanov, IHEP, Protvino, Russia (2002).

[69] A. Gasparyan, private communication.